14 Surface Physics

M. Hengsberger, R. Westerström, L. Castiglioni, H. Cun, G. Mette, E. Miniussi,
S. Förster, C. Monney, D. Leuenberger, L. H. de Lima, R. Stania, C. Bernard,
A. Kostanyan, A. Schuler, W.-D. Zabka, P. Kliuiev, K. Waltar, Y. Kubota,
M. Baumgartner, M. Graf, T. Stöckli, T. Kälin, T. Greber, and J. Osterwalder

For the investigation of surface and interface phenomena at the atomic level, our laboratory is well equipped for the preparation and characterization of clean single-crystalline surfaces, metal and molecular monolayer films, as well as sp^2-bonded single layers on surfaces, using a wide variety of experimental techniques. In addition, we are part of a user consortium of the soft x-ray beam-line *PEARL (PhotoEmission and Atomic Resolution Laboratory)* at the Swiss Light Source. Our group has further built and commissioned a compact and mobile angle-resolved photoemission (ARPES) instrument, to be used at advanced laser sources within the NCCR *Molecular Ultrafast Science and Technology (MUST)*, while a second ARPES spectrometer is currently being set up together with a high-harmonic gas jet source for producing high-energy UV light.

The research carried out during the report period can be grouped into four topics:

- 2D Materials
  Monolayer hexagonal boron nitride (h-BN) and graphene are grown by chemical vapor deposition (CVD) on metal surfaces. Using well controlled ultrahigh vacuum (UHV) conditions and single-crystal metal films as substrates, we are in a position to grow these 2D materials in a single crystalline domain. A strong effort has been made to optimize methods for de-laminating these films from their metal substrate, in order to explore further their transport properties in the case of graphene, or their applicability for nanofiltration purposes in the case of h-BN. Sec. 14.1 presents some first promising results for monolayer graphene transferred from the Ir(111) substrate onto an amorphous and insulating SiO_2 film.

- Ultrafast processes at surfaces
  Charge transfer processes upon optical excitation of adsorbed molecules are studied by time-resolved two-photon photoemission (2PPE). Specifically, a visible pump pulse populates the lowest unoccupied molecular orbital (LUMO), which can be detected in photoemission by a second, delayed photon. The goal is to extract lifetimes and charge transfer rates from the observed transients. In a second project the motion of adsorbed molecules is addressed by time-resolved photoelectron diffraction. A first successful proof-of-principle study of this type, showing coherent phonon excitation in Bi(111), is discussed in Sec. 14.3.

- Adsorbed molecular catalysts and photosensitizers
  Within the University Research Priority Program *Light to Chemical Energy Conversion* (LightChEC) our role is to develop and study model catalyst surfaces for solar water splitting. Currently these are based on pyrphyrin ligands (see Sec. 14.2) that we have learned to immobilize on Au(111) and TiO_2(110) surfaces, where the Co-metalated molecules readily form upon Co evaporation. Rhenium-based photosensitizers are grafted onto ultrathin alumina films of various thicknesses via covalent bonds. This is achieved by self-assembly from solution. For this purpose, a chamber with a liquid reservoir has been built from which the sample can be transferred directly into our UHV system for further preparation and characterization. The goal is to measure charge transfer times via tunneling through the alumina film.

- Spin shuttles
  Endohedral single molecule magnets (*spin shuttles*) of the type $RE_3N@C_{80}$ where RE are one, two or three different rare earth ions (e.g. $Dy_2ScN@C_{80}$) offer a broad variety of magnetic behavior at low temperatures. In a collaboration with IFW Dresden (A. Popov) and PSI Villigen (C Piamonteze) the magnetic and structural properties of these largely unexplored systems are studied by means of SQUID magnetometry and x-ray magnetic circular dichroism (XMCD).

In the following, three highlights of last year's research are presented in more detail.

14.1 Large-scale transfer of single-crystal graphene from Ir thin films

In collaboration with: Benjamin Probst, Chemistry Department, Universität Zürich; Miroslav Haluska, Micro- and Nanosystems, D-MAVT, ETH Zürich.

In the framework of the European Flagship for Future and Emerging Technologies (FET) 'GRAPHENE', we investigate the growth of single crystalline boron nitride and graphene (g). In–situ chemical vapour deposition (CVD) is an established method for the synthesis of high–quality epitaxial graphene on the close–packed surfaces of many transition metals. An alternative to expensive and size–limited bulk single crystals is offered by twin-free, single crystal films of metals of the Pt group grown on YSZ-buffered Si(111) substrates [1]. We are able to synthesize single-domain graphene films on 150 nm–thick Ir(111)/YSZ/Si(111) four–inch wafers [2]. In comparison with graphene synthesis on metal foils (e.g. copper), which implies growth of multiple domains, this method leads to large–area graphene flakes with a crystalline orientation matching that of the substrate.

For most applications in electronics and nanotechnology, however, graphene needs to be transferred onto an insulating substrate, typically SiO_2. An alternative to the traditional chemical etching of the metal substrate is offered by the electrochemical delamination of the graphene sheet (*bubbling*) [3]. This method performs very well for graphene on platinum and copper [4,5], but until recently only limited transfer rates could be achieved for graphene transferred from Ir thin films. We made progress in this respect by introducing an additional step in the transfer protocol, as reported by L. Koefoed *et al.* [6]. While Raman spectra indicate a high defect concentration in the graphene layer, we are able to directly measure the average charge carrier density by photoemission.

Figure 14.1 shows the Raman spectrum of single crystalline graphene on an amorphous SiO_2 film and a Fermi surface map from this sample. Clearly, the six Dirac cones of graphene appear at the corners of the Brillouin zone, though rather smeared out, likely due to the presence of local charges and roughness effects on the insulating substrate. Nevertheless the carrier density can be inferred from such data. The photoemission result directly indicates large scale single crystallinity, since the photon beam in our instrument has a diameter of about 2 mm. This opens the doors to many more experiments on two-dimensional materials other than graphene, where the electrons may be directly observed in reciprocal space.

[1] S. Gsell *et al.*, J. Cryst. Growth **311**, 3731 (2009).

[2] A. Hemmi *et al.*, Rev. Sci. Instrum. **85**, 035101 (2014).

[3] G. Lupina *et al.*, ACS Nano **9**, 4776 (2015).

[4] Y. Wang *et al.*, ACS Nano **5**, 9927 (2011).

[5] L. Gao *et al.*, Nature Commun. **3**, 699 (2012).

[6] L. Koefoed *et al.*,
   J. Phys. D: Appl. Phys. **48**, 115306 (2015).

FIG. 14.1 –
(a) Schematics of the TOA-assisted electrochemical delamination procedure.
(b) Raman spectra of the transferred samples (excitation wavelength: 532 nm) acquired in a high– and low–defect density region, respectively.
(c) Fermi surface map of g/SiO$_2$ acquired with He IIα radiation.
(d) Background-subtracted azimuthal scan acquired with He IIα radiation along the K-K' direction normalized by the Fermi function. The Fermi level obtained from the fit, as well as the valence and conduction bands, simulated via a basic tight-binding model, are superimposed.
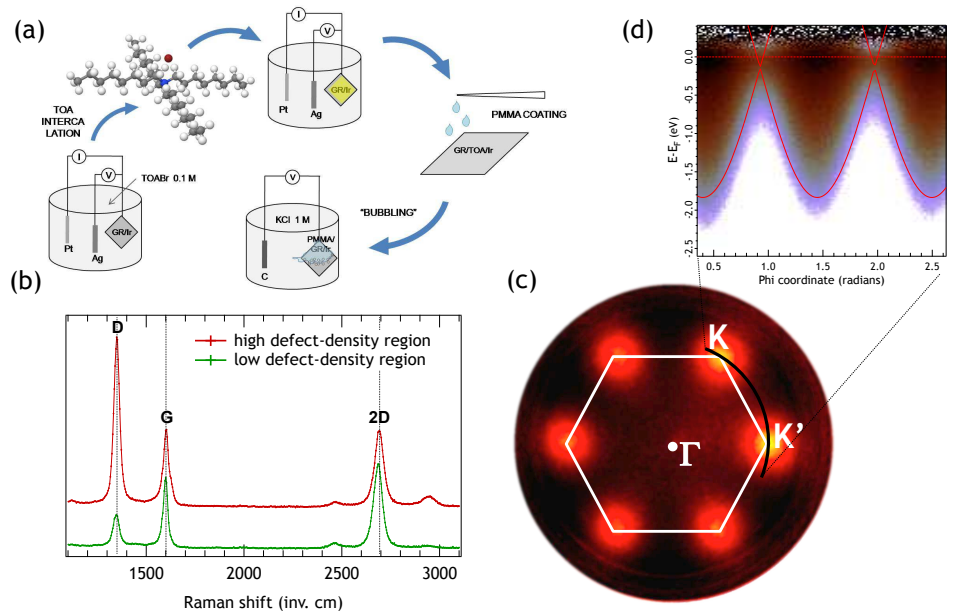
14.2 Adsorption and metalation of pyrphyrin on Au(111)

In collaboration with:
Yeliz Gurdal, Stephan Schnidrig, Benjamin Probst, Marcella Iannuzzi, Jürg Hutter and Roger Alberto, Chemistry Department, Universität Zürich.

Metal complexes based on pyrphyrin ligands have recently shown promise as water reduction catalysts in homogeneous photo-chemical water splitting reactions [7]. We have studied the adsorption of pyrphyrin on a single crystalline surface and examined its controlled metalation in ultra-high vacuum (UHV) [8]. Coverages up to one monolayer were obtained by sublimation of the molecules on a Au(111) surface kept at room temperature. Deposition of Co metal at the level of 5% of a monolayer and subsequent annealing then led to the formation of 90% of Co-pyrphyrin (CoPyr) molecules.

Fig. 14.2 - left shows an STM image of the hexagonally-ordered Pyr molecules which appear donut-shaped with a weak indication of two-fold symmetry. After Co deposition at a sample temperature of 323 K (Fig. 14.2 - center), most of the molecules have maintained their donut shape, but some of them appear brighter and exhibit two distinct lobes. Successive annealing up to 423 K increases the number of brighter molecules, but their contrast changes from the two lobes to a single central protrusion (Fig. 14.2 - right). The metalation thus appears to be temperature driven. After the Co evaporation, one part of the Co atoms assembles in clusters that are observed in STM scans over a larger area, whereas another part is already ligated to the cores of Pyr molecules. Due to the annealing, on the one hand Co atoms dissociate from the initially formed clusters and diffuse along the surface, before they are captured by Pyr molecules. On the other hand, the changing sub-molecular contrast of the Co-ligated Pyr species indicates the existence of an intermediate state (CoPyr-2H) prior to the annealing.

Our assignments are corroborated by of XPS measurements and density functional theory (DFT) calculations. The N 1s spectra in Fig. 14.3 directly probe the local chemistry within the pyrphyrin molecules. Due to the three types of chemical environment of N atoms within the free-base molecule, pyridinic (-NH-), iminic (-C=N-) and cyano (-C≡N) nitrogen, the spectrum of Pyr/Au(111) (top panel) can be well fitted with three components. After Co evaporation and subsequent annealing of the sample (bottom spectrum), the spectrum seemingly collapses into a single peak. It can be fitted with four components, a major one at 399.2 eV, a smaller one at the cyano nitrogen position forming the shoulder, as well as two small remnant pyridinic and iminic components, reflecting few unmetalated molecules. Co deposition without annealing yields a distinct shift of the N 1s spectra to higher binding energies (middle spectrum). The 4-component does not lead to a satisfactory fit and, to account for the probable CoPyr-2H intermediate, two additional nitrogen components (the light-blue and light-green curves) were introduced in the N 1s model. The reaction steps for the Co metalation of a monolayer of pyrphyrin molecules on Au(111) could thus be established.

[7] E. Joliat, *et al.*, *Dalton Trans.* **45**, 1737 (2016).

[8] G. Mette *et al.*, *Nanoscale* **8**, 7958 (2016).
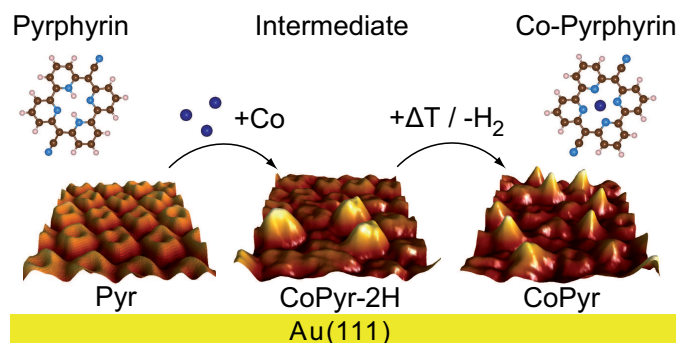

FIG. 14.2 – STM images of free-base pyrphyrin molecules (left), after deposition of cobalt at 323 K (center), and after annealing the surface to 423 K (right).
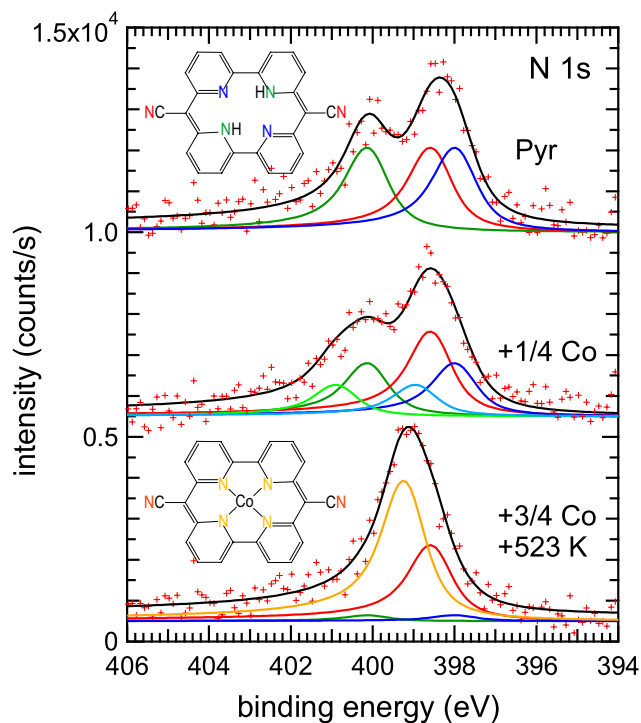

FIG. 14.3 – XPS data and corresponding fits of N 1s spectra before the Co evaporation (top), after partial Co evaporation without annealing (middle) and after the complemented Co evaporation with subsequent annealing to 523 K (bottom).

14.3 Structural dynamics studied by time-resolved photoelectron diffraction

In collaboration with:
Lamia Kasmi, Matteo Lucchini, Lukas Gallmann and Ursula Keller, Physics Department, ETH Zürich; NCCR MUST.

Coherent phonons are an excellent tool to investigate the interplay between electronic and structural dynamics. The displacive excitation of coherent phonons in elemental bismuth is one of the most widely studied processes for this purpose. In a simple model, phonons are kick-started coherently by a short pulse promoting electrons into unoccupied states and shifting the atomic equilibrium positions. As a consequence of the electronic response to the lattice modulation, the phonon mode drives an oscillation of the electronic charge density. The phase lag between the forced oscillation and the driving force is determined by the ratio of friction represented by the electron population decay rate and the phonon frequency. We employed time-resolved photoelectron diffraction to access the structural dynamics by recording the energy-integrated valence photoemission intensity as function of emission angle.

Photoelectrons excited by absorption of x-ray or extreme ultraviolet (XUV) light will undergo scattering processes at nearest-neighbors of the emitter atoms. The resulting interference pattern carries information about the local environment of the emitter [9]. The time-resolved structural response of a solid after excitation with an intense infrared pump pulse can thus be monitored by photoelectron diffraction produced by XUV probe pulses. The temporal resolution in such a pump-probe experiment is determined by the cross correlation of the pump and probe light pulses.

In Fig. 14.4(a) the photoemission yield from emission from the valence band close to the Fermi energy E_F is shown as function of time delay for three different high-symmetry points in the surface Brillouin zone. At time delay zero a steep increase in intensity can be seen as a consequence of the excitation of electrons to unoccupied states above E_F. The increase is followed by an exponential decay. On top of the decay an intensity modulation is observed with a period of about 360 fs or a frequency of 2.76 THz.

The generation of the hot-electron gas at delay zero can be modeled by decoupling electronic and lattice temperature; assuming thermal equilibrium within the electron gas only, the excess energy of the electron gas can be converted into a formal electronic temperature of about 2000 K [11, 12]. The modulations were already investigated previously with tr-ARPES and attributed to transient changes in the bulk electronic structure caused by the coherent excitation of A_{1g} phonons [11]. We performed tight-binding calculations [13] once for the equilibrium lattice and once for the distorted lattice corresponding to the maximum A_{1g} amplitude of 0.04 Å expected for the fluence used here [14, 15] (Fig. 14.4(b)). The so-called photoemission density of states (DOS) is then obtained by integrating the density of states over a small volume in reciprocal space which matches the solid angle covered by the detector and is centered at the initial state momenta where the photo-excitation takes place. The calculations indeed predict a *decrease* of the DOS near the L-point upon increasing distortion away from the rhombohedral and towards the simple cubic lattice. Thus, the photoemission intensity modulation shows a minimum for maximum distortion at half a phonon period. This explains why the modulation phase is such that the increasing edge is followed by a minimum and then by a maximum at about 360 fs (bottom two curves in Fig. 14.4(a)).
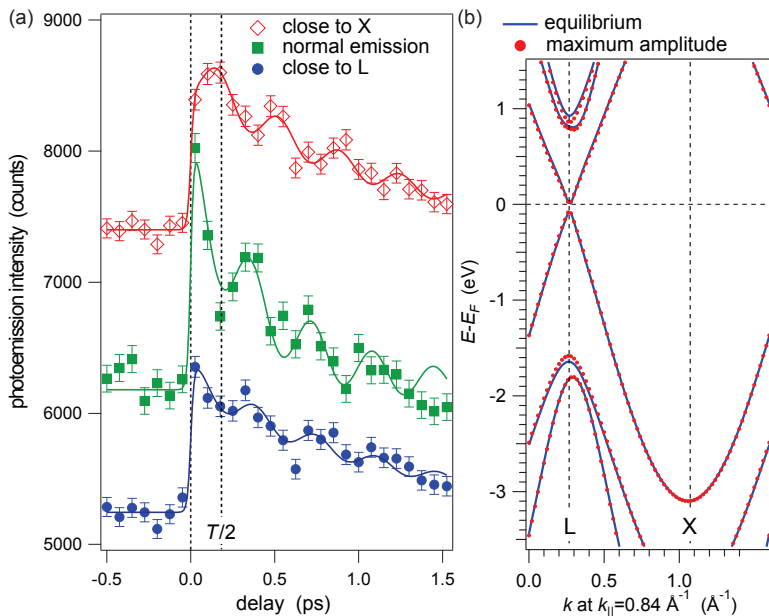
FIG. 14.4 – Time- and angle-resolved photoemission from Bi(111) after absorption of an intense IR pump pulse.
(a) Integrated valence band intensity as function of time delay for normal emission $\overline{\Gamma}$ (ΓT-line) and the $\overline{M}$ (L) and $\overline{M}'$ (X) points at the border of the first surface (bulk) Brillouin zone.
(b) Tight-binding calculation of the band structure for the bulk L- and X-points.

FIG. 14.5 –

(a) SSC calculation of the photo-electron diffraction pattern for the Bi(111) surface: upper part difference excited-equilibrium, lower part equilibrium structure. The blue arrow indicates the measurement position for the data in the right panel. (b) Comparison of two diffraction transients (green and blue symbols) and the intensity recorded at the bulk X-point (red symbols). The curves are fits to the data.

58
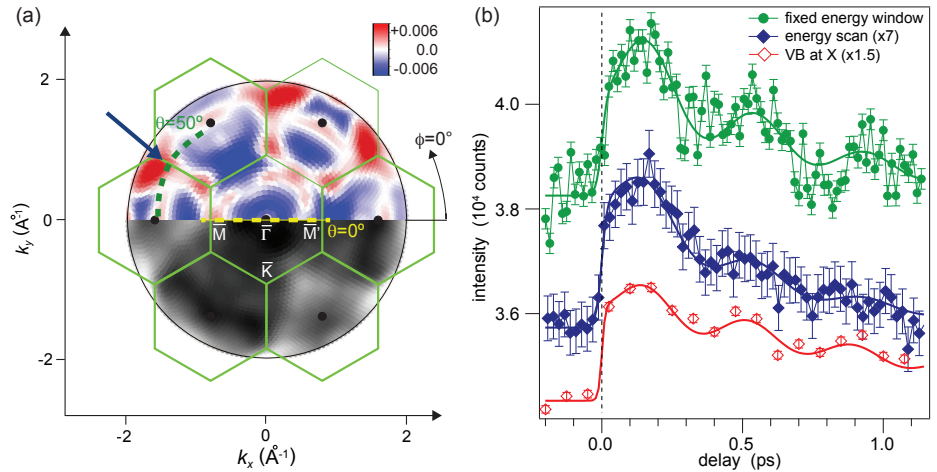
In contrast to L, the X-point exhibits a large energy gap around E_F. The time-dependent photoemission intensity at X is dominated by photoelectron diffraction effects. The structural distortion by the A_{1g} mode leads to a change in distance between emitter and scatterer along the [111]-axis and, thereby, to a displacement of the interference fringes. Depending on the solid angle sampled in the experiment, this shift of the fringes results in an increase or decrease in photoemission intensity. Single-scattering cluster (SSC) calculations show that an increase of photoemission intensity at angles corresponding to emission from the X-point is expected for increasing lattice distortion, as can be seen in stereographic representation in Fig. 14.5(a). This explains the shift of about 2.8 rad between the intensity modulations at the X-point ($\overline{M}$) and at the $\overline{\Gamma}$- or L-point ($\overline{M}'$).

Further strong diffraction effects can be found at the emission angle $\theta = 50°$ in the direction indicated by the blue arrow in Fig. 14.5(a). The valence band yield measured at this angle is shown as function of time delay in Fig. 14.5(b) and compared to the spectral intensity recorded at the X-point. At time delay zero, a slow increase is observed reaching maximum intensity after half a phonon period. The phase offset of the cosine function is close to that of the modulation at $\overline{M}$. The average phase lag of $\varphi \approx 2.80$ rad appears to be significantly smaller than π with respect to the electronic excitation. In order to elucidate this large difference, we estimate the decay time constant necessary to obtain the observed phase shift based on a semi-classical

model of Zeiger et al. [10]. The experimental values lead to a value close to the thermalization time $\tau_e(\overline{\Gamma}) = 0.44$ ps of the initial hot-electron distribution. This suggests that the early dynamics of the hot electrons determine the phase lag between electrons and phonons. Indeed, the nuclear acceleration due to the large initial displacement of electronic charge density is expected to be stronger than for the subsequent phonon cycles. At the same time, the initial hot electron distribution decays fast leading to an initial overshooting and over-damping of the A_{1g} mode, which yet is fluence dependent as evidenced by our experimental data.

 [9] M. Greif et al., Phys. Rev. B **87**, 085429 (2013).

[10] H. J. Zeiger et al., Phys. Rev. B **45**, 768 (1992).

[11] E. Papalazarou et al.,
     Phys. Rev. Lett. **108**, 256808 (2012).

[12] D. Leuenberger et al.,
     Phys. Rev. Lett. **110**, 136806 (2013).

[13] Y. Liu and R.E. Allen, Phys. Rev. B **52**, 1566 (1995).

[14] D.M. Fritz et al., Science **315**, 633 (2007).

[15] G. Sciaini et al., Nature **457**, 56 (2009).